



OPEN

SUBJECT AREAS:

SENSORS AND
BIOSENSORS

LAB-ON-A-CHIP

MAGNETIC PROPERTIES AND
MATERIALS

ASSAY SYSTEMS

Magnetoresistive performance and comparison of supermagnetic nanoparticles on giant magnetoresistive sensor-based detection system

Wei Wang*, Yi Wang*, Liang Tu, Yinglong Feng, Todd Klein & Jian-Ping Wang

Department of Electrical and Computer Engineering, University of Minnesota, Minneapolis, MN 55455, USA.

Received
20 January 2014Accepted
12 June 2014Published
21 July 2014

Correspondence and requests for materials should be addressed to J.-P.W. (jpwang@umn.edu)

* These authors contributed equally to this work.

Giant magnetoresistive (GMR) biosensors have emerged as powerful tools for ultrasensitive, multiplexed, real-time electrical readout, and rapid biological/chemical detection while combining with magnetic particles. Finding appropriate magnetic nanoparticles (MNPs) and its influences on the detection signal is a vital aspect to the GMR bio-sensing technology. Here, we report a GMR sensor based detection system capable of stable and convenient connection, and real-time measurement. Five different types of MNPs with sizes ranging from 10 to 100 nm were investigated for GMR biosensing. The experiments were accomplished with the aid of DNA hybridization and detection architecture on GMR sensor surface. We found that different MNPs markedly affected the final detection signal, depending on their characteristics of magnetic moment, size, and surface-based binding ability, etc. This work may provide a useful guidance in selecting or preparing MNPs to enhance the sensitivity of GMR biosensors, and eventually lead to a versatile and portable device for molecular diagnostics.

In recent years, technologies for biomolecular diagnostics using hand-held, easy-to-use, point of care (POC), and economical lab-on-a-chip type devices have attracted the interest of biotechnological companies and the scientific community. However, widely used POC devices for individuals are still limited to simple diagnostics like pregnancy testing and glucose monitoring. Different kinds of ultra-sensitive biosensors have been designed and developed¹⁻⁷. Chip-based detection of biological agents using giant magnetoresistive (GMR) sensors and magnetic labels have emerged recently⁸⁻¹⁶, and this GMR sensing technology has the merits of low cost, portability, high sensitivity, and real-time electronic readout. In addition, the fabrication of GMR sensors is compatible with the current large-scale integration technologies, so GMR sensors can be easily integrated and their cost can be greatly reduced as mass production is carried out.

The working principle for GMR sensing is detecting stray magnetic field introduced by bound magnetic labels on sensor surface, and magnetic labels are usually functionalized magnetic micro- or nano-particles. GMR biosensors require the specific labeling on magnetic particles, which have been widely used in separation of proteins and cells, hyperthermia, and drug delivery¹⁷⁻¹⁹. Labeling of different biomolecules ranging from small molecules (some drugs) to large molecules (antibodies) is compatible on particle surface and has been successfully demonstrated in these processes. Traditionally, magnetic particles with diameters of between 0.3 μm and 3 μm ²⁰⁻²⁵ were used with GMR sensor systems, but these magnetic labels are too large to suppress the dissociation of bound biomolecules from sensor surface. This means that kinetic studies of molecules interaction using large magnetic particles for GMR sensor would not be accurate, and large particles hinder high-density binding across the sensor surface. They are undesirable because micro-particles would have a much larger effect on the output signal than nanoparticles as non-specific binding event occurs. Wang and co-workers²⁶ have developed a GMR sensing based model for kinetic analysis of proteins interaction, which is more sensitive in detection limit and has wider dynamic range than surface plasmon resonance (SPR) technologies. In their work, magnetic nanoparticles (MNPs) with sizes of about 50 nm were employed, and this kind of MNPs is comparable in size to some biomolecules like proteins and DNA. It indicates that small magnetic labels do much better than large magnetic labels in kinetic studies. Mulvaney²⁷ inferred that kinetic studies with GMR sensors will be accurate when the MNPs diameter is less than a critical value. As an indispensable key player in GMR biosensor system, MNPs not

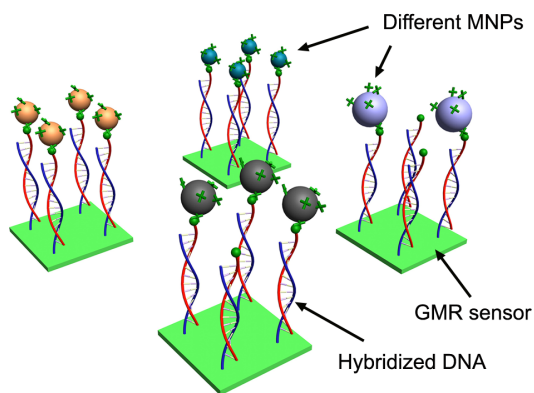


Figure 1 | Schematic representation of DNA hybridization on GMR sensors and binding with different MNPs.

only affect the kinetic studies but also is one of the influential factors on GMR biosensor besides sensor fabrication, surface functionalization, and system setup, etc.

In this paper, five kinds of water-soluble MNPs with the diameter ranging from 10 to 100 nm were selected (see Supplementary Table S1), and they were measured and compared using a GMR sensor based detection system.

Results

The experiments were accomplished with the aid of DNA hybridization and detection architecture on GMR sensor surface (Figure 1). The chip with 64 GMR sensors was fabricated by a photolithography technique²⁸. The layout and size for the chip and sensor are shown in Figure 2 and Supplementary Fig. S1. The 64 sensors were symmetrically arranged in an 8×8 array, and this would be convenient for automatic spotting with biomolecules in sensor surface functionalization. The sizes of one GMR chip and one sensor are about 16×16 mm and 120×120 μm respectively. One chip can have up to 64 sensors, taking into account of sensors spacing and layout of connecting wires. However, this is not the limit of sensors on one GMR chip, and GMR sensors could be scaled to over 100,000 sensors per cm^2 ²⁶. The magnetic orientation of pinned layer is aligned to the minor axis and a typical GMR sensor has a magnetoresistive ratio (MR) of 2.6% after post annealing (Supplementary Fig. S2). The easy axis of the free layer is along the long strip due to shape anisotropy. The transfer curve has a linear part in the range of -50 Oe to 50 Oe, which is desired for GMR bio-sensing. With aid of sc-FLEXARRAYER S5 printing system, bovine serum albumin (BSA) and probe DNA solutions can be robotically spotted on each sensor (Supplementary Fig. S3). This printing capability promotes multiplex protein or oligonucleotide detection which requires the application of different receptor to different sensor. Many of proteins or oligonucleotides binding experiments would be run in one shot on one GMR chip. Microfluidic technique is usually employed to introduce sample solution to sensor surface, and it has been used in GMR biosensor²⁹. However, microfluidics needs an external pump system. Pap pen has also been used to draw film-like barriers on microscope slides to stop solution spreading, but it is not suitable for small-scale GMR chip and the contact lines may be scratched during drawing. Herein a reaction well was used to hold solution so that the reagents can be easily pipetted and aspirated.

The whole GMR sensor based detection system is shown in Supplementary Fig. S4. The GMR sensor is fixed in a reusable chip holder, while a probe array connects the GMR sensor with the PCB. Also it is cheap and can be reused thousands of times. The top hole allows easy loading and aspirating samples, as well as washing in real-time measurements. Before building DNA hybridized architectures on the sensor surface, we tried DNA hybridization experiments on

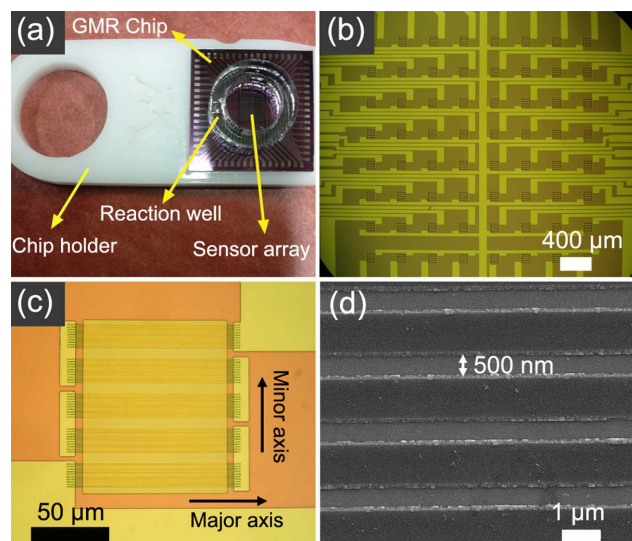


Figure 2 | (a) GMR chip with attached reaction well was placed on the chip holder. The size of GMR chip is about 16×16 mm. (b) 8×8 sensor array in the center area of GMR chip, and the distance between adjacent sensors is 400 μm . (c) Optical image of one GMR sensor. One sensor has 50 strips which consist of 5 strip groups in series and each group has 10 strips connected in parallel. The dimension of one strip is about 120 $\mu\text{m} \times 750$ nm. (d) The strips in parallel. The gaps between strips were filled with SiO_2 in order to prevent MNPs from being attracted into the sidewalls of the strips. Some parts on two sides of strip are also covered by SiO_2 , so the width of one strip is actually 500 nm.

silicon wafer with same functionalized surface as that of GMR sensor. Unlike traditional colorimetric assay, fluorescence dye labeled streptavidin was directly used to replace enzyme labeled streptavidin which required further substrates addition. The fluorescent spots (Supplementary Fig. S6) suggest that target DNA has been successfully hybridized onto probe DNA immobilized surface. These spots are round and red-color imaged against a low background. The fluorescent signal increases as the concentration of probe DNA goes up from 0.1 to 50 nmol/mL, and the signal appears to be saturated at the concentration of 50 nmol/mL. Thus, 50 nmol/mL of probe DNA was used in hybridization experiments on GMR sensor.

Magnetic moment per particle versus applied external magnetic field at room temperature is shown in Supplementary Fig. S7 and Fig. S8. No obvious coercivity is observed for all the five kinds of MNPs, confirming their superparamagnetic property. The saturation magnetic moment values (M_s) and magnetic moment values at 30 Oe ($M_{30\text{Oe}}$) for different MNPs are listed in Table 1. It is apparent that the M_s value per particle increases with an increase in the particle size as expected, because particles with bigger size contains a higher volume of magnetic materials. The $M_{30\text{Oe}}$ value for 50 nm MNPs is 2.3×10^{-15} emu which is even larger than that for 100 nm MNPs. This may be due to the fact that they are prepared by different approaches and have different microstructures.

For the detection of signal, the bound MNPs are magnetized by the applied alternating in-plane field, and the stray field from MNPs can be detected by the GMR sensor as an output signal. Frequency of the alternating in-plane field plays an important role in the magnetizing process of MNPs. There could be Brownian and/or Néel relaxation mechanisms for MNPs under different alternating magnetic field. The two relaxations depend on the effective hydrodynamic volume and magnetic volume, respectively. They are also two driving forces in the application of magnetic particle hyperthermia^{30,31}. Both Brownian and Néel relaxation times for the five different types of MNPs are estimated and listed in Supplementary Table S2. Generally Brownian relaxation dominates when the diameter of MNPs is larger

Table 1 | The measured and calculated signals per particle for different MNPs^a

MNPs (diameter)	M_s (10^{-16} emu)	$M_{30\text{Oe}}$ (10^{-16} emu)	$A1$ (10^{-18} emu/(nm) ^{1.3})	$A2$ (10^{-20} emu/(nm) ^{1.3})	B (Measured Signal, 10^{-6} μV)
10 nm	0.82	0.02	0.38	0.94	2.42
20 nm	7.8	1.1	3.3	46.5	15.1
30 nm	10.8	1.05	4.16	40.43	22.1
50 nm	81	23	26.33	747.77	177.08
100 nm	368	18	84.65	414.07	305.56

^aAll the values listed above are calculated for one particle. The measured signal per MNP (B) is calculated from bound numbers of MNPs, size of sensor ($120 \times 120 \mu\text{m}$), and measured signal. We statistically assume that all the MNPs are ideally bound uniformly and every MNP has the same contribution to signal. $A1 = M_s / (\text{radius} + 57 \text{ nm})^{1.3}$, $A2 = M_{30\text{Oe}} / (\text{radius} + 57 \text{ nm})^{1.3}$. It is assumed that the bound number for the 10 nm MNPs is $230/\mu\text{m}^2$.

than 20 nm. However, it is not necessarily true for the MNPs bound on sensor surface because the viscosity (η) has dramatically increased, leading to the increase of Brownian relaxation time, or even they cannot show any Brownian rotation. In the GMR detection system, the magnetization of bound MNPs should keep pace with the frequency of the alternating in-plane field, otherwise the contribution of bound MNPs to the detection signal could not be fully used. The magnetization of MNPs in solution is measured under the alternating field by using a mixing-frequency method³², and the results are presented in Supplementary Fig. S9. The 50 and 100 nm MNPs show no obvious phase lagging along the high frequency, and it means that Néel relaxation dominates for the MNPs with a magnetic core size of 10 nm. It can be inferred that amplitude of the 10 nm, 50 nm and 100 nm bound MNPs magnetization has no big difference during the detecting process (50 Hz) on the GMR system. Under low frequency (<100 Hz), both Brownian and Néel relaxations work for the 20 nm MNPs as they are dispersed in solution. However, Brownian relaxation dominates for the 30 nm MNPs which have a very large Néel relaxation time. It is impossible for the magnetization of the immobilized MNPs to flip under an AC magnetic field if they cannot rotate or move. Therefore, the magnetization of bound 30 nm MNPs might not be fully used for signal generation in the measurement. It's critical to determine the optimal frequency of the external applied field. If the frequency is too high, it may bring problems like magnetic coil heating and phase lagging of MNPs. If the frequency is too low, it may increase the system noise due to $1/f$ noise.

The real-time binding curves (signal vs. time) for five different kinds of MNPs are shown in Figure 3a, and MNPs are added at 10 min. The flat curves from 0 to 10 min indicate that the system is stable with low background noise. Any drift or jumping would interfere with the detection signals. Beginning at $t = 10$ min, the signals for all the five kinds of MNPs show a rise, reflecting that MNPs are binding to the sensor surface in real-time. As expected, the signal for the control sensor does not show an obvious rise throughout the whole measuring process. This means that MNPs are rarely non-specifically bound to the sensor surface. It also indi-

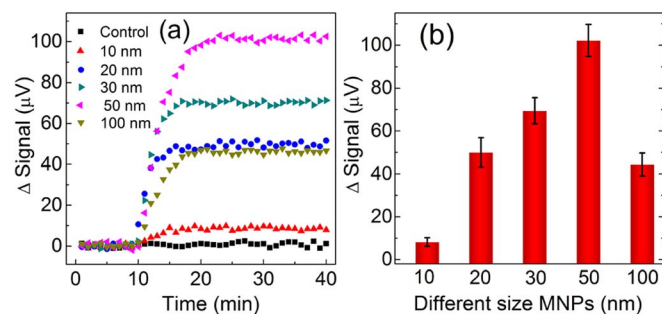


Figure 3 | (a) Typical binding curve data in real time and (b) average final signals (with standard deviation) for different MNPs.

cates that other non-biological binding factors, such as electronics and temperature drift, etc, don't influence the readout signal much. The MNPs bindings reach equilibrium within 10 min, and it appears that the signal saturates within 5 min for 10 nm MNPs. Compared with large-size MNPs, small-size MNPs have a stronger Brownian motion, which may speed up MNPs diffusion and binding. It is apparent that their saturated signal levels vary greatly, and their average overall signals are presented in Figure 3b. The 50 nm MNPs generate the highest signal among the five kinds of MNPs under the same testing condition, and it has an average signal of 102 μV . In contrast, the average signal for 10 nm MNPs is dramatically reduced to 8 μV . The 20 nm, 30 nm and 100 nm MNPs bring the signals of 50, 70 and 44 μV respectively. Under specific detection condition, the final readout signal is dependent on not only the characteristics of MNPs but also the number of bound MNPs.

SEM results (Figure 4) show that few MNPs were bound on the control sensor surface that was covered by BSA, and this is consistent with the signal for the control sensor. BSA is a negatively charged protein³³, and all the five kinds of MNPs are also negatively charged at pH 7.4 (Supplementary Table S1). The electrostatic repulsion can prevent the MNPs from non-specifically binding onto the control sensor. Application of the MNPs onto probe DNA oligonucleotides immobilized surface was attempted, and we found few MNPs were bound. This makes sense because the DNA strands are negatively charged by their phosphate/sugar backbones. It can be also inferred that the MNPs would not non-specifically bind to a sensor surface after the hybridization of biotinylated target DNA oligonucleotides has been completed. Figure 4b–4f show the GMR sensor surfaces with bound MNPs. The low-magnification images are also presented in Supplementary Fig. S10. 10 nm MNPs are too small to be visualized after the sensor surface is metalized with 5 nm Au, so it is not shown here. The 20 nm and 30 nm MNPs are densely and uniformly bound on sensor surfaces, and they are well dispersed and agglomeration is seldom observed. The bound numbers for the 20 nm and 30 nm MNPs are $230/\mu\text{m}^2$ and $220/\mu\text{m}^2$ respectively. The numbers have drastically decreased for the 50 nm and 100 nm MNPs (40 and

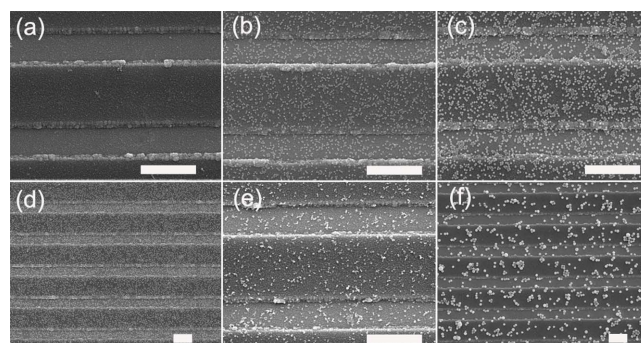


Figure 4 | SEM images of different MNPs bound on GMR sensor surface. (a) Control; (b) 20 nm MNPs; (c) 30 nm MNPs; (d) 30 nm MNPs (Zoom out); (e) 50 nm MNPs; (f) 100 nm MNPs. All the scale bars are 1 μm .



$10/\mu\text{m}^2$). They are not uniform in distribution and appear with frequent multi-particle clusters. It can be inferred from the bound number of 20 nm MNPs that there are at least 230 binding sites per μm^2 on sensor surface after DNA hybridization. The maximal accommodated numbers for the 50 nm and 100 nm MNPs are 400 and $100/\mu\text{m}^2$, respectively, if they ideally form a compact monolayer on the sensor surface. Thus, most of the binding sites are not occupied for the 50 nm and 100 nm MNPs, which show a lower biological binding ability than the 20 nm and 30 nm MNPs for the detection condition.

Discussion

By virtue of its advantages, GMR biosensor as a robust analytical tool has great potential to be a versatile and portable device for molecular diagnostics eventually. As one of the key parts of GMR biosensor platform, MNPs are significantly vital to the detection capability. In our experiments, it makes a big difference in final signals as various kinds of MNPs used. Some vital characteristics of MNPs should be taken into consideration. According to previous study³⁴, the surface charges of MNPs and sensor affect MNPs approaching and binding. Positively charged MNPs can be electrostatically attracted to negatively charged planar surface. In contrast, MNPs with highly negative charge do not show any kind of binding to the negatively charged surface, even through specific binding of “biotin-streptavidin”. Thus, the characteristic of surface charge for MNPs should be taken into account depending on target analytes and detection technique. Even though the companies providing the MNPs claim that they have an excellent binding ability to biotin or biotinylated molecules, they are designed for solution-based applications and especially have succeeded in biological separation and purification. The biotin binding capacity may not be true to surface-based application like GMR biosensing. Recognizing a target on sensor surface is generally considered to be more difficult due to a limited diffusion rate and steric hindrance³⁵. The real output signal for one MNP is listed in Table 1. Larger MNPs provide larger signal per particle as expected. However, by taking the surface-based binding ability into account, 30 nm and 50 nm MNPs produce higher overall signal than 100 nm MNPs under the given condition.

In GMR bio-sensing, the signal generated by one bound MNP is proportional to the average MNP stray field generated along the axis of the fixed reference layer. The position of this single MNP on the sensor can then be adjusted many times to obtain an array of these average stray fields. This array of results can be averaged once more to obtain a signal that represents the stray field induced by a typical MNP landing in some random location. The twice-averaged stray field is proportional to the MNP moment derived from the Langevin Function where the total field acting on the MNP must include the applied field and magnetostatic fields from GMR film layers. Finally, we can generate a result for each value of applied field to derive the AC measurement result. With this information, we can estimate a distance-relationship for specific situations. In the case that we use our specific sensor geometry, we obtain a (roughly) $m/d^{1.3}$ relationship. Here, m is the dipole magnetic moment of MNP, and d is the distance between the center of MNP and surface of free layer. This distance (d) is the sum of 5 nm of Ta layer, 25 nm of Al_2O_3 , 20 nm of SiO_2 , 7 nm of hybridized DNA architecture, and radius of MNP. The saturation magnetic moment values (M_s) and moment values at 30 Oe ($M_{30\text{Oe}}$) for the MNPs are both investigated and their $m/d^{1.3}$ are also calculated (Table 1). The Pearson correlation coefficient (r) between measured signal and $M_s/d^{1.3}$ is 0.96, indicating a strong positive correlation between them. The r between measured signal and $M_{30\text{Oe}}/d^{1.3}$ is 0.75, showing a positive correlation too. Overall, MNPs with high magnetic moment are desired in GMR biosensors.

In summary, choosing the MNPs is a vital aspect of the GMR biosensing technology. The most important characteristics of MNPs used in GMR biosensors are magnetic moment, size, and surface-

based binding ability. Other characteristics, such as stability, surface charge, and responding to frequency of magnetic field, etc, should be also considered in specific detection condition. The majority of magnetic particles being used now are iron oxides. Compared to iron oxides, FeCo MNPs with the same size exhibit much higher magnetic moment. Our previous study¹¹ shows that FeCo MNPs had excellent performance in magnetic biosensors. Therefore, the best solution we are studying now is imbedding a cluster of small FeCo into polymer to form large MNP. This will increase the magnetic content of each MNP while remaining superparamagnetic, and engineering its surface to increase the surface-based binding ability.

Methods

GMR sensor fabrication and surface functionalization. GMR biochip with 64 sensors was designed and fabricated, and the multi-layer stack was top-down composed of Ta (50 Å)/NiFe (20 Å)/CoFe (10 Å)/Cu (33 Å)/CoFe (25 Å)/IrMn (80 Å)/Ta (25 Å), which was fabricated by a Shamrock Sputtering System. An anti-ferromagnetic IrMn layer was used to pin the fixed magnetic CoFe layer, and the free layer consisted of CoFe and NiFe bi-layers. Protective bi-layers of 25 nm Al_2O_3 and 20 nm SiO_2 were finally coated on chip surface. The chip was annealed at 200°C for 1 h under 4.5 kOe magnetic field and the field orientation was along minor axis of GMR sensor. The magnetic orientation of pinned layer could be fixed along the minor axis after annealing treatment. Before biomolecules immobilization on the GMR sensor surface, the sensors surface was functionalized by 3-aminopropyltriethoxy silane and glutaraldehyde²⁸.

DNA hybridization. The probe DNA oligonucleotide (5′/ACAAACAACGGAAACCAGCA/3AmM6T/3′) with amino modification was purchased from Integrated DNA Technologies, Inc. It (50 nmol/mL) was spotted on GMR sensors, and some sensors in the same chip were spotted with BSA (10 mg/mL) and were used as control sensors (Supplementary Fig. S3). The printed GMR chip was incubated for 24 h at room temperature under a relative humidity of ~90%, followed by being rinsed with 0.2% SDS solution and ultrapure water. For inactivating surplus aldehyde groups and reducing non-specific binding, 1.0 mg NaBH₄ was dissolved in 400 μL PBS (1×) and 100 μL ethanol, and the resulted solution was added on chip surface and incubated for 5 min. After three washes with ultrapure water, the chip was immersed in hot water for several minutes to denature any annealed DNA. The chip was rinsed thoroughly with ultrapure water and dried by a stream of nitrogen. A reaction well made of polymethyl methacrylate (PMMA) was attached onto chip surface. The reaction well can help to load a maximal liquid volume of 100 μL on sensor array area.

Biotinylated target DNA oligonucleotide (5′/TGCTGGTTCCGGTTGTTTGT/BiotinBB-/3′, 50 nmol/mL, 100 μL , purchased from TriLink Biotechnologies) containing 4× SSC + 0.2% SDS + 0.2 mg/mL BSA was preheated to 42°C and immediately loaded into reaction well. After being incubated for 3 h at 37°C, the chip was washed with 2× SSC + 0.2% SDS and ultrapure water, followed by being dried by nitrogen gas.

Detection system setup. A Data Acquisition Card (DAQ) NI USB-6289 is used as an analog output signal generator and an input signal digitizer. Two analog output channels are used to generate pilot tones for circuit and coil driver. One DAC input channel is used to digitize signal with 18 bit and 500 kS/s. When operating in the minimum voltage range ± 100 mV, digitization has the highest accuracy of 28 μV and highest sensitivity of 0.8 μV . The input and output channels of the DAQ shares the same clock source so frequency and phase jitter can be effectively avoided. Although the input channel has a built-in low pass filter, multiple analog low pass filters are integrated in the circuit to suppress the noise sources, especially from the output channel of DAQ. The GMR sensor arrays are addressed by Multiplexers ADG1606 and are measured in time sequence. Each chip has 16 bi-directional single channels, and the switch of each channel is determined by the 4-bit binary address lines fed by the digital output channel of DAQ. All the GMR sensors share one Wheatstone bridge setup. The Wheatstone bridge can dramatically eliminate the background analog signal, thus the small meaningful signal can be amplified and detected. An instrumentation amplifier INA163 is used as a final stage signal amplifier. The gain is adjusted by a potentiometer to fit the optimal range of the DAQ input channel.

Signal measurement. 30 μL PBS solution was preload into reaction well in order to make sensor surface with hybridized DNA transfer from dry to wet. An alternating current at 1 KHz was applied to each sensor after the chip was connected to the system. An alternating in-plane field of 30 Oe at 50 Hz was applied along the minor axis of the sensor. The amplitude at mixing tones (1000 \pm 50 Hz) is measured as primary signal by a Fast Fourier Transform of the time-domain voltage signal from the DAQ. By implementing ac current and field, the mixing tones can effectively avoid the 1/f noise and the interference. Each measure takes one second and amplitude and phase are recorded continuously in real time. After running for 10 min, 30 μL of MNPs solution was added, and the detection signal generated by MNPs binding to sensor surface could be real-time recorded. As the signal measurement was finished, the GMR chip was taken out and washed by water to



remove any unbound MNPs, followed by being dried by nitrogen gas. For the 100 nm MNPs, they were easier to get away from the sensor surface. Thus, we immersed the GMR chip with bound 100 nm MNPs into water solution and stirred slightly, and unbound MNPs would be dispersed into water. N₂ drying was not used for this chip and we just let the surface dry naturally. Then the chip was coated with 5 nm Au film and further investigated by Field Emission Scanning Electron Microscopy (FESEM, JEOL 6500). Five different types of MNPs were tested herein, and their detailed information was listed (Supplementary Table S1). All the five types of MNPs had been functionalized with streptavidin which could specifically bind to the biotin labeled on probe DNA oligonucleotide.

- Hodnik, V. & Anderluh, G. Toxin Detection by Surface Plasmon Resonance. *Sensors*. **9**, 1339–1354 (2009).
- Zheng, G., Patolsky, F., Cui, Y., Wang, W. U. & Lieber, C. M. Multiplexed Electrical Detection of Cancer Markers with Nanowire Sensor Arrays. *Nat. Biotechnol.* **23**, 1294–1301 (2005).
- Shao, H. *et al.* Protein typing of circulating microvesicles allows real-time monitoring of glioblastoma therapy. *Nat. Med.* **18**, 1835–1841 (2012).
- Nam, J. M., Thaxton, C. S. & Mirkin, C. A. Nanoparticle-Based Bio-Bar Codes for the Ultrasensitive Detection of Proteins. *Science*. **301**, 1884–1886 (2003).
- Martinez, A. W., Phillips, S. T. & Whitesides, G. M. Diagnostics for the Developing World: Microfluidic Paper-Based Analytical Devices. *Anal. Chem.* **82**, 3–10 (2010).
- Cheng, Y. *et al.* Functionalized SnO₂ nanobelt field-effect transistor sensors for label-free detection of cardiac troponin. *Biosens. Bioelectron.* **26**, 4538–4544 (2011).
- Gao, A. R. *et al.* Silicon-Nanowire-Based CMOS-Compatible Field-Effect Transistor Nanosensors for Ultrasensitive Electrical Detection of Nucleic Acids. *Nano Lett.* **11**, 3974–3978 (2011).
- Gordon, J. & Michel, G. Discerning Trends in Multiplex Immunoassay Technology with Potential for Resource-Limited Settings. *Clin. Chem.* **58**, 690–698 (2012).
- Baselt, D. R., Lee, G. U., Natesan, M., Metzger, S. W., Sheehan, P. E. & Colton, R. J. A biosensor based on magnetoresistance technology. *Biosens. Bioelectron.* **13**, 731–739 (1998).
- Rife, J. C., Miller, M. M., Sheehan, P. E., Tamanaha, C. R., Tondra, M. & Whitman, L. J. Design and performance of GMR sensors for the detection of magnetic microbeads in biosensors. *Sensor. Actuat. A-Phys.* **107**, 209–218 (2003).
- Srinivasan, B. *et al.* A detection system based on giant magnetoresistive sensors and high-moment magnetic nanoparticles demonstrates zeptomole sensitivity: potential for personalized medicine. *Angew. Chem. Int. Ed.* **48**, 2764–2767 (2009).
- Osterfeld, S. J. *et al.* Multiplex protein assays based on real-time magnetic nanotag sensing. *P. Natl. Acad. Sci.* **52**, 20637–20640 (2008).
- Schotter, J., Kamp, P. B., Becker, A., Puhler, A., Reiss, G. & Bruckl, H. Comparison of a prototype magnetoresistive biosensor to standard fluorescent DNA detection. *Biosens. Bioelectron.* **19**, 1149–1156 (2004).
- Graham, D. L., Ferreira, H. A. & Freitas, P. P. Magnetoresistive-based biosensors and biochips. *Trends. Biotechnol.* **22**, 455–462 (2004).
- Xu, L. *et al.* Giant magnetoresistive biochip for DNA detection and HPV genotyping. *Biosens. Bioelectron.* **24**, 99–103 (2008).
- Zhi, X., Liu, Q., Zhang, X., Zhang, Y., Feng, J. & Cui, D. Quick genotyping detection of HBV by giant magnetoresistive biochip combined with PCR and line probe assay. *Lab Chip*. **12**, 741–745 (2012).
- Jun, Y. W., Seo, J. W. & Cheon, J. Nanoscaling laws of magnetic nanoparticles and their applicabilities in biomedical sciences. *Acc. Chem. Res.* **41**, 179–189 (2008).
- Bae, K. H. *et al.* Chitosan oligosaccharide-stabilized ferrimagnetic iron oxide nanocubes for magnetically modulated cancer hyperthermia. *ACS Nano*. **6**, 5266–5273 (2012).
- Kong, S. D. *et al.* Magnetically Vectored Nanocapsules for Tumor Penetration and Remotely Switchable On-Demand Drug Release. *Nano Lett.* **10**, 5088–5092 (2010).
- Koets, M., van der Wijk, T., van Eemeren, J. T., van Amerongen, A. & Prins, M. W. Rapid DNA multi-analyte immunoassay on a magneto-resistance biosensor. *Biosens. Bioelectron.* **24**, 1893–1898 (2009).
- Schotter, J., Shoshi, A. & Brueckl, H. Development of a magnetic lab-on-a-chip for point-of-care sepsis diagnosis. *J. Magn. Magn. Mater.* **321**, 1671–1675 (2009).
- Mulvaney, S. P. *et al.* Rapid, femtomolar bioassays in complex matrices combining microfluidics and magnetoelectronics. *Biosens. Bioelectron.* **23**, 191–200 (2007).

- Manteca, A., Mujika, M. & Arana, S. GMR sensors: magnetoresistive behaviour optimization for biological detection by means of superparamagnetic nanoparticles. *Biosens. Bioelectron.* **26**, 3705–3709 (2011).
- Miller, M. M. *et al.* A DNA array sensor utilizing magnetic microbeads and magnetoelectronic detection. *J. Magn. Magn. Mater.* **225**, 138–144 (2001).
- Martins, V. C. *et al.* Femtomolar limit of detection with a magnetoresistive biochip. *Biosens. Bioelectron.* **24**, 2690–2695 (2009).
- Gaster, R. S. *et al.* Quantification of protein interactions and solution transport using high-density GMR sensor arrays. *Nat. Nanotechnol.* **6**, 314–320 (2011).
- Mulvaney, S. P. Magnets tackle kinetic questions. *Nat. Nanotechnol.* **6**, 266–267 (2011).
- Wang, W., Wang, Y., Tu, L., Klein, T., Feng, Y. & Wang, J. P. Surface modification for Protein and DNA immobilization onto GMR biosensor. *IEEE Trans. Magn.* **49**, 296–299 (2013).
- Loureiro, J. *et al.* Magnetoresistive Detection of Magnetic Beads Flowing at High Speed in Microfluidic Channels. *IEEE Trans. Magn.* **45**, 4873–4876 (2009).
- Fortin, J. P., Gazeau, F. & Wilhelm, C. Intracellular heating of living cells through Néel relaxation of magnetic nanoparticles. *Eur. Biophys. J.* **37**, 223–228 (2008).
- Mamiya, H. & Jeyadevan, B. Hyperthermic effects of dissipative structures of magnetic nanoparticles in large alternating magnetic fields. *Sci. Rep.* **1**, 157 (2011).
- Tu, L., Jing, Y., Li, Y. & Wang, J. P. Real-time measurement of Brownian relaxation of magnetic nanoparticles by a mixing-frequency method. *Appl. Phys. Lett.* **98**, 213702 (2011).
- Salgin, S., Salgin, U. & Bahadir, S. Zeta Potentials and Isoelectric Points of Biomolecules: The Effects of Ion Types and Ionic Strengths. *Int. J. Electrochem. Sci.* **7**, 12404–12414 (2012).
- Palma, R. D. *et al.* Magnetic Particles as Labels in Bioassays: Interactions between a Biotinylated Gold Substrate and Streptavidin Magnetic Particles. *J. Phys. Chem. C* **111**, 12227–12235 (2007).
- Stenberg, M. & Nygren, H. Kinetics of antigen-antibody reactions at solid-liquid interfaces. *J. Immunol. Methods*. **113**, 3–15 (1988).

Acknowledgments

This work was partially supported by the U.S. Department of Defense under the Ovarian Cancer Translational Pilot Award, Institute of Engineering in Medicine seed grant, Office for Technology Commercialization (OTC) Innovation grant and the resident fellows grant of the Institute on the Environment (IonE) at the University of Minnesota. Parts of this work were carried out in the Characterization Facility, University of Minnesota, which receives partial support from National Science Foundation through the MRSEC program.

Author contributions

J.P.W. coordinated the overall research. W.W., Y.W. and J.P.W. developed concept and designed research; W.W., Y.W., L.T., Y.F. and T.K. performed research and collected data; W.W., Y.W., L.T. and J.P.W. analyzed data; and W.W., Y.W. and J.P.W. wrote the paper. All authors discussed the results and implications and commented on the manuscript at all stages. All authors reviewed the manuscript.

Additional information

Supplementary information accompanies this paper at <http://www.nature.com/scientificreports>

Competing financial interests: The authors declare no competing financial interests.

How to cite this article: Wang, W. *et al.* Magnetoresistive performance and comparison of supermagnetic nanoparticles on giant magnetoresistive sensor-based detection system. *Sci. Rep.* **4**, 5716; DOI:10.1038/srep05716 (2014).



This work is licensed under a Creative Commons Attribution-NonCommercial-NoDerivs 4.0 International License. The images or other third party material in this article are included in the article's Creative Commons license, unless indicated otherwise in the credit line; if the material is not included under the Creative Commons license, users will need to obtain permission from the license holder in order to reproduce the material. To view a copy of this license, visit <http://creativecommons.org/licenses/by-nc-nd/4.0/>